

Supporting Information

High-Performance Electrochemical Catalysts Based on Three-Dimensional Porous Architecture with Conductive Interconnected Networks

Dong Wang,^{†, ‡, §} Jie Wang,^{‡, §} Zi-en Liu,[‡] Xiangdong Yang,[‡] Xiaoxia Hu,[‡] Jinqi Deng,[‡] Nianjun Yang,^{†, ⊥} Qijin Wan,^{, †} and Quan Yuan^{*, ‡}*

[†]School of Chemistry and Environmental Engineering, Wuhan Institute of Technology, Wuhan 430073, China

[‡]Key Laboratory of Analytical Chemistry for Biology and Medicine (Ministry of Education), College of Chemistry and Molecular Sciences, Wuhan University, Wuhan 430072, China

[⊥]Institute of Materials Engineering, University of Siegen, Siegen 57076, Germany

Corresponding author

*E-mail: qijinwan@wit.edu.cn, yuanquan@whu.edu.cn

[§]D. Wang and J. Wang contributed equally to this work.

Chemicals

Bisphenol A (BPA, $\geq 99.8\%$), potassium tetrachloroplatinate (K_2PtCl_4 , $\text{Pt} > 40\%$), potassium chloropalladite (K_2PdCl_4 , $\text{Pd} \geq 32.6\%$), chloroauric acid ($\text{HAuCl}_4 \cdot 4\text{H}_2\text{O}$, $\text{Au} > 47.8\%$), tris(hydroxymethyl)aminomethane ($\text{C}_4\text{H}_{11}\text{NO}_3$, $\geq 99.5\%$), potassium hexacyanoferrate (III) ($\text{K}_3\text{Fe}(\text{CN})_6$, $\geq 99\%$), potassium hexacyanoferrate (II) ($\text{K}_4\text{Fe}(\text{CN})_6 \cdot 3\text{H}_2\text{O}$, $\geq 99.5\%$), potassium chloride (KCl , AR), sodium hydroxide (NaOH , AR), sulfuric acid (H_2SO_4 , AR), sodium dihydrogen phosphate dehydrate ($\text{NaH}_2\text{PO}_4 \cdot 2\text{H}_2\text{O}$, AR), sodium phosphate dibasic ($\text{Na}_2\text{HPO}_4 \cdot 12\text{H}_2\text{O}$, AR), sodium chloride (NaCl , AR), p-benzenediol ($\text{C}_6\text{H}_6\text{O}_2$, $\geq 99\%$), 1,2-benzenediol ($\text{C}_6\text{H}_6\text{O}_2$, $\geq 99\%$), 1,3-benzenediol ($\text{C}_6\text{H}_6\text{O}_2$, $\geq 99\%$), porous polymer (Al_2O_3 , $0.05\mu\text{m}$) were purchased from Sinopharm Chemical Reagent Co. (Shanghai China). Chitosan ($(\text{C}_6\text{H}_{11}\text{NO}_4)_n$, BR), diethylstilbestrol ($\text{C}_{18}\text{H}_{20}\text{O}_2$, $\geq 99\%$), 4-nonylphenol ($\text{C}_{15}\text{H}_{24}\text{O}$, $\geq 85\%$), 2-octylphenol ($\text{C}_{14}\text{H}_{22}\text{O}$, $\geq 99\%$), tris(2-Carboxyethyl)phosphine hydrochloride (TCEP, $\geq 99.8\%$), 6-mercapto-1-hexanol ($\text{C}_6\text{H}_{14}\text{OS}$, $\geq 99.8\%$) were obtained from Aladdin.

Aptamers

BPA binding aptamer was synthesized on an ABI3400 DNA/RNA synthesizer (Applied Biosystems, Foster City, CA, USA) and further purified with reversed-phase HPLC (Agilent, 1260 Infinity Quaternary, Japan).

BPA binding aptamer: 5'-SH-TTT TTT TTT CCG GTG GGT GGT CAG GTG GGA TAG CGT TCC GCG TAT GGC CCA GCG CAT CAC GGG TTC GCA CCA-3'

Instruments

Transmission electron microscopy (TEM) images were taken from A JEM-2100 transmission electron microcopy (JEOL, Japan) with a working voltage of 200 kV. Scanning electron microscopy (SEM) images were obtained from a Hitachi S-4800 microscope (Hitachi, Japan). X-ray photoelectron spectroscopy (XPS) analysis was performed on an ESCALAB 250Xi XPS spectrometer (Thermo Fisher, U.K.) with 225 W of Al K α radiation. An ASAP 2010 analyzer (Micromeritics) was used to measures the nitrogen adsorption and desorption isotherms of all porous materials. A Nikon D3000 digital single-lens reflex camera (Japan) was used for recording photographs. Electrochemical measurements were performed on a CHI 760E electrochemical working station (Shanghai Chenhua, China) with a conventional three-electrode system at room temperature. A saturated calomel electrode (SCE) acted as the reference electrode and a platinum foil as the counter electrode. The CHI 760E electrochemical working station was used for cyclic voltammetry (CV), differential pulse voltammetric (DPV) measurements and electrochemical impedance spectroscopy (EIS). The EIS measurements were performed in 0.1 M KCl solution containing 5 mM [Fe(CN) $_6$] $^{3-/4-}$. The amplitude of the applied sine wave potential was 5 mV. The impedance measurements were recorded at a bias potential of 190 mV within the frequency range of 1 Hz to 10 kHz.

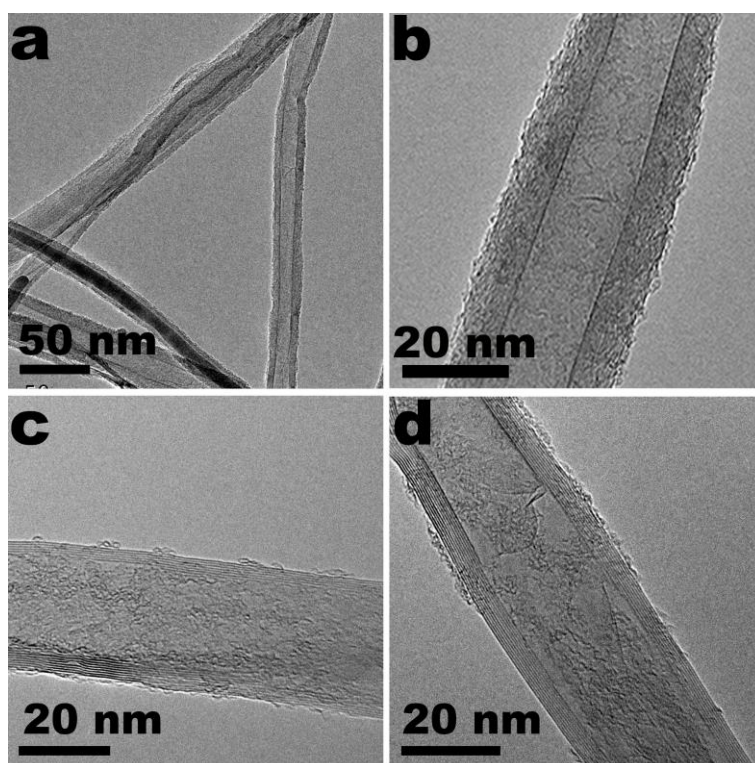


Figure S1. (a-d) TEM images of CNT sponge at different magnifications.

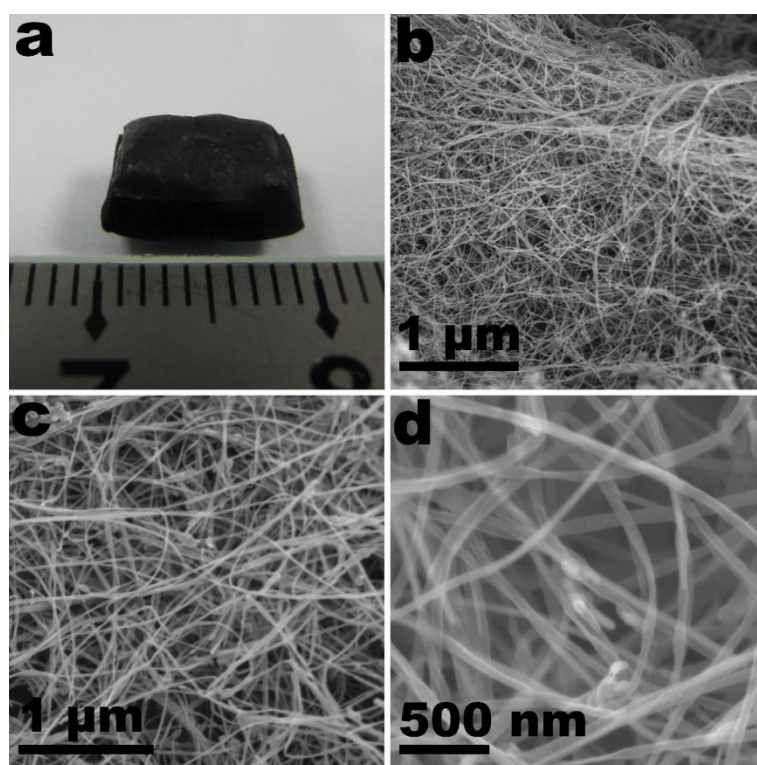


Figure S2. Photograph of CNT sponge (a). SEM images of CNT sponge at different magnifications (b-d).

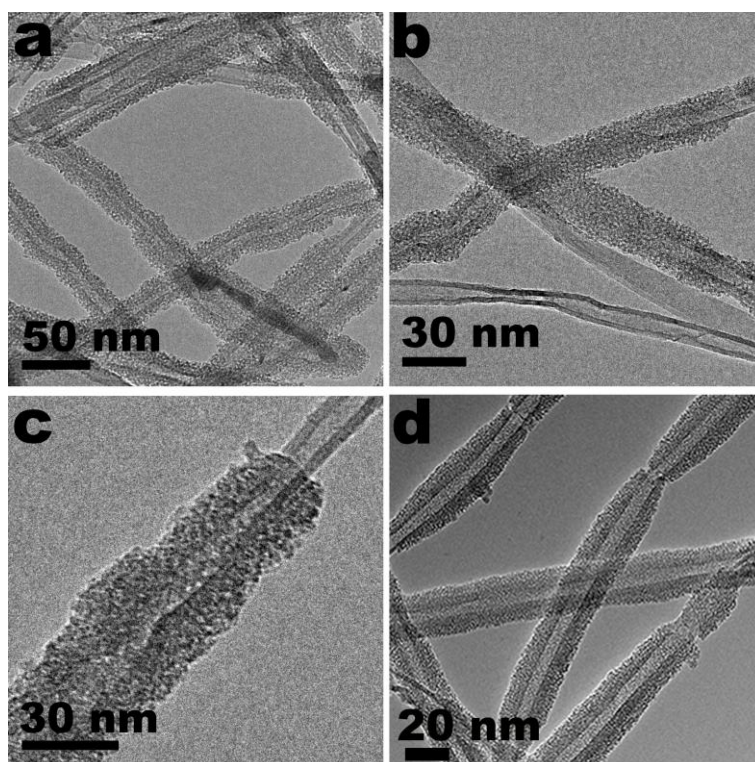


Figure S3. (a-d) TEM images of CNT@mSiO₂ at different magnifications.

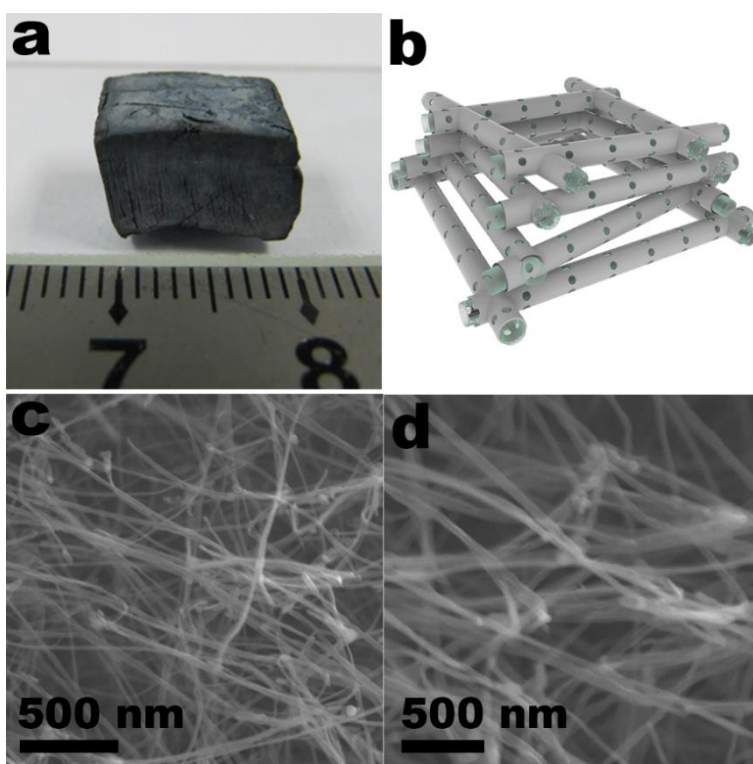


Figure S4. Photograph (a) and schematic illustration (b) of CNT@mSiO₂ sponge. SEM images of CNT@mSiO₂ sponge at different magnifications (c, d).

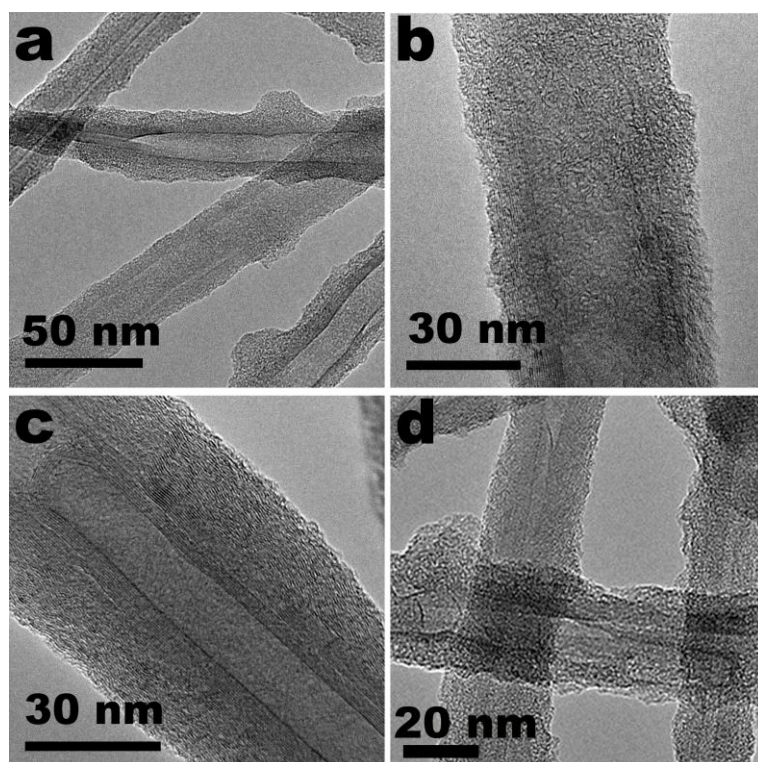


Figure S5. (a-d) TEM images of CNT@mC at different magnifications.

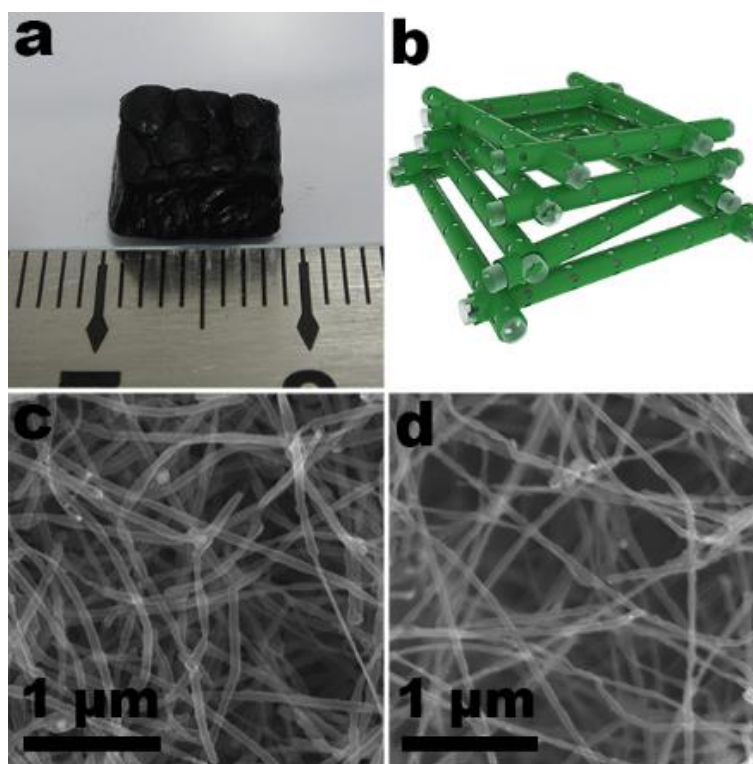


Figure S6. Photograph (a) and schematic illustration (b) of CNT@mC composite sponge. SEM images of CNT@mC composite sponge at different magnifications (c, d).

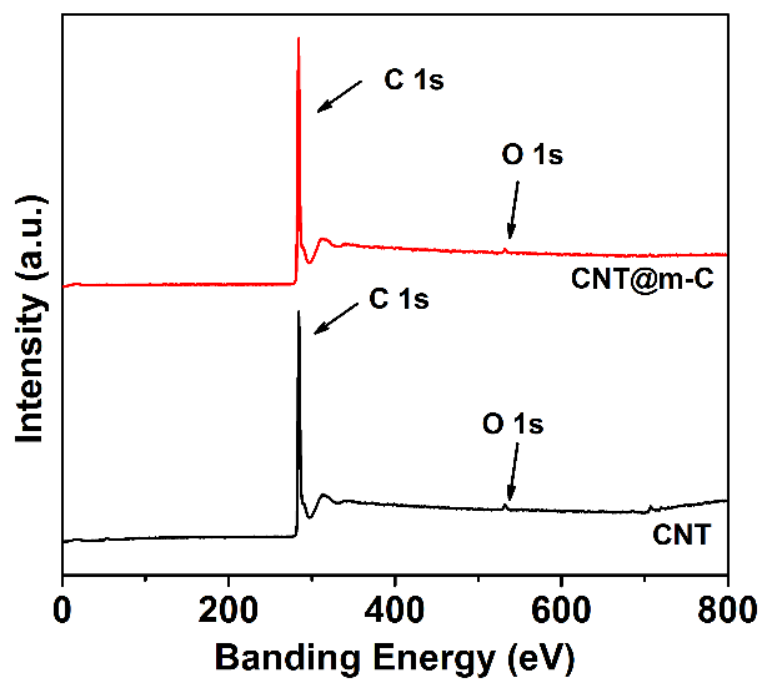


Figure S7 XPS spectra of the original CNT sponge and CNT@mC composite sponge.

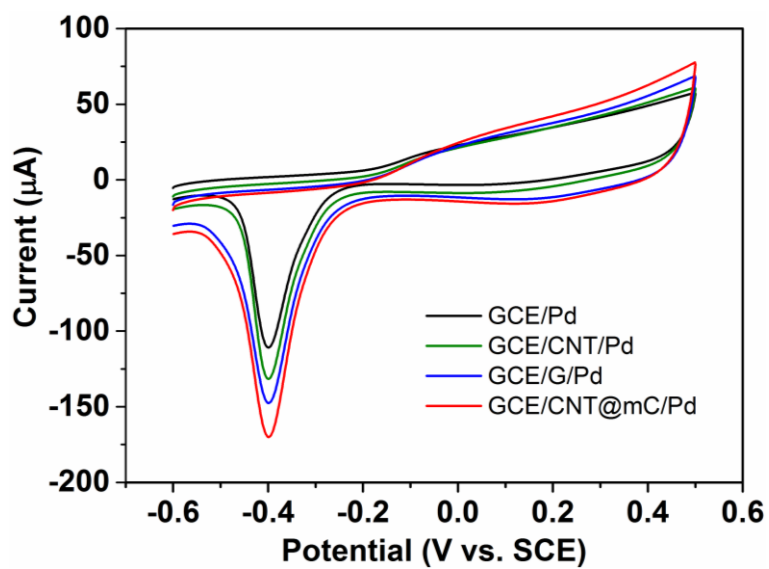


Figure S8. Cyclic voltammograms of GCE/Pd, GCE/CNT/Pd, GCE/G/Pd, and GCE/CNT@mC/Pd in NaOH solution (0.1 M) at scan rate of 100 mV s^{-1} .

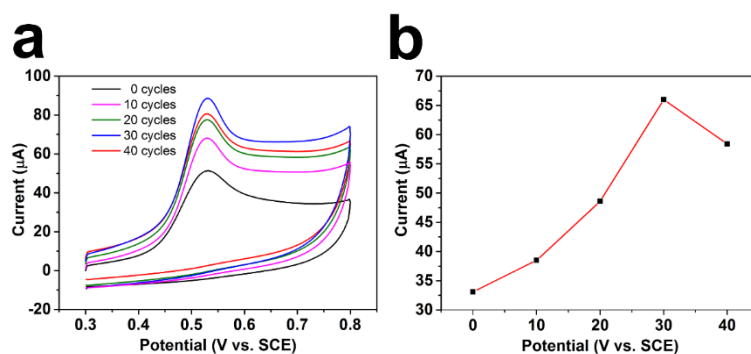


Figure S9. (a) Cyclic voltammograms of CH_3OH on the GCE/CNT@mC/Pd with different amounts of Pd loading. (b) The corresponding peak currents of methanol oxidation at different amounts of Pd loading.

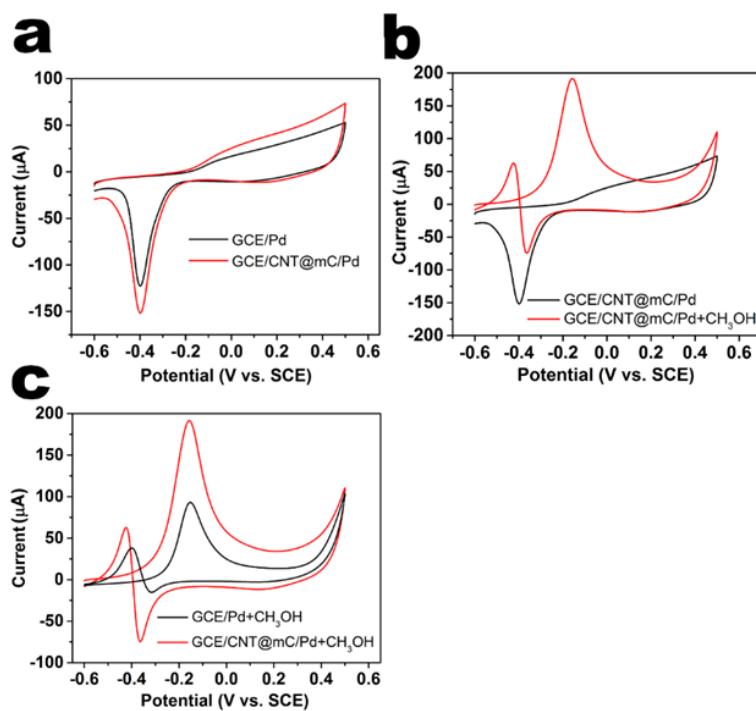


Figure S10. (a) Cyclic voltammograms of GCE/Pd and GCE/CNT@mC/Pd in 0.1 M NaOH at scan rate of 100 mV s^{-1} . (b) Cyclic voltammograms of GCE/CNT@mC/Pd and GCE/CNT@mC/Pd in 0.1 M NaOH solution containing 0.1 M CH_3OH at scan rate of 100 mV s^{-1} . (c) Cyclic voltammograms of GCE/Pd and GCE/CNT@mC/Pd in 0.1 M NaOH solution containing 0.1 M CH_3OH at scan rate of 100 mV s^{-1} .

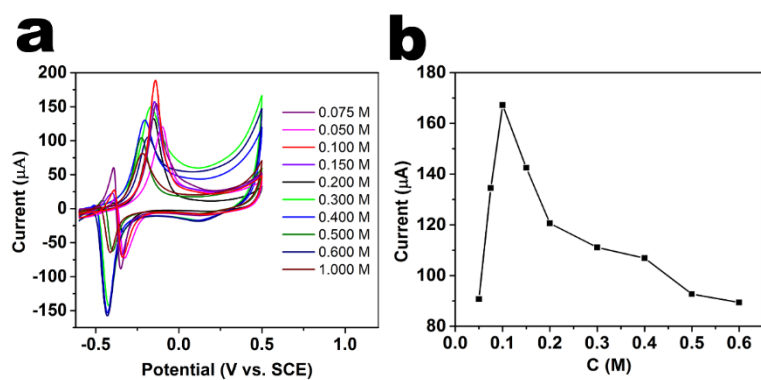


Figure S11. (a) Cyclic voltammograms of CH₃OH (0.1 M) at GCE/CNT@mC/Pd in NaOH solutions with different concentrations. (b) The corresponding oxidation peak currents obtained in NaOH solution with different concentrations.

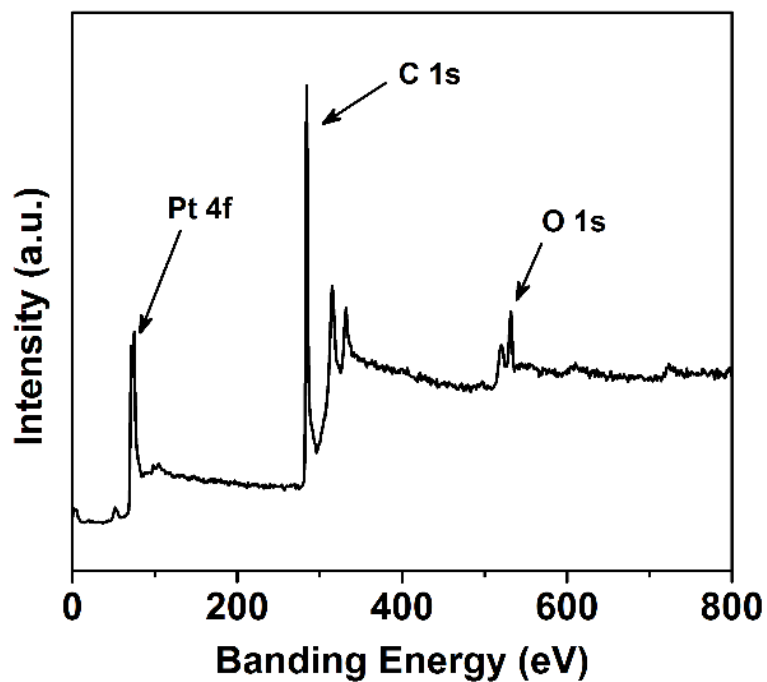


Figure S12. XPS spectra of CNT@mC/Pt.

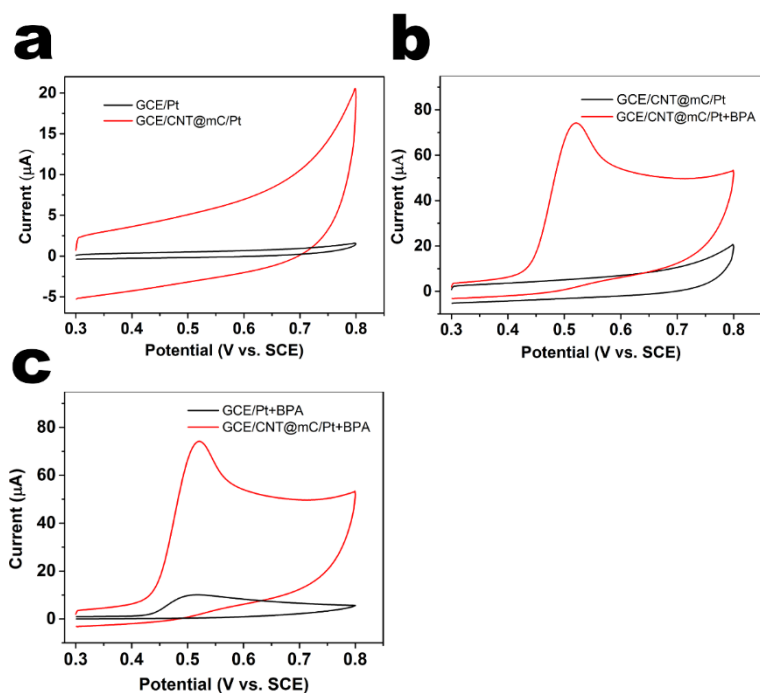


Figure S13. (a) Cyclic voltammograms of GCE/Pt and GCE/CNT@mC/Pt in PBS buffer at scan rate of 100 mV s⁻¹. (b) Cyclic voltammograms of GCE/CNT@mC/Pt and GCE/CNT@mC/Pt in PBS buffer containing BPA (1.0 mM) at scan rate of 100 mV s⁻¹. (c) Cyclic voltammograms of GCE/Pt and GCE/CNT@mC/Pt in PBS buffer containing BPA (1.0 mM) at scan rate of 100 mV s⁻¹.

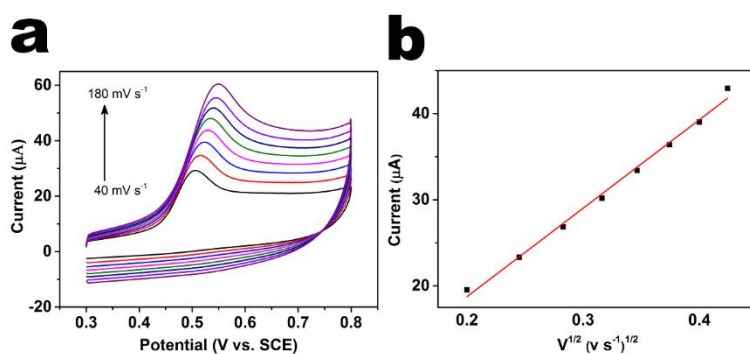


Figure S14. (a) Cyclic voltammograms of the GCE/CNT@mC/Pt electrode in PBS buffer containing BPA (1.0 mM) at different scan rates. (b) The linear relationship between BPA oxidation currents with $v^{1/2}$ at scan rates from 40 to 180 mV s⁻¹.

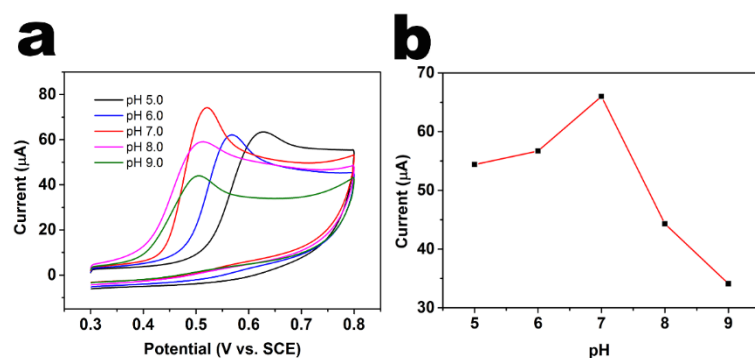


Figure S15. (a) Cyclic voltammograms of BPA (1.0 mM) on GCE/CNT@mC/Pt at different pH values. (b) The corresponding BPA oxidation currents at different pH values.

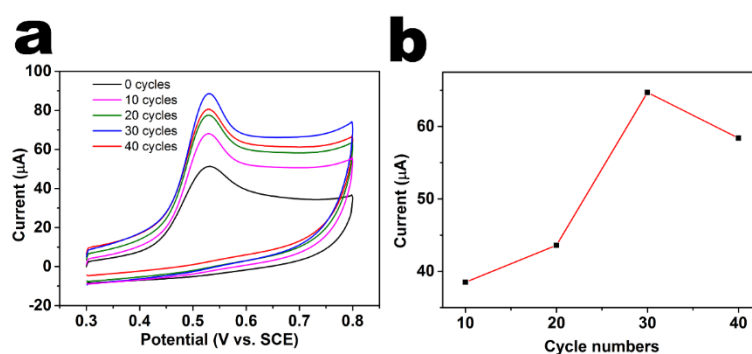


Figure S16. (a) Cyclic voltammograms of BPA (1 mM) on GCE/CNT@mC/Pt with different amounts of Pt loading. (b) The corresponding BPA oxidation currents with different amounts of Pt loading.

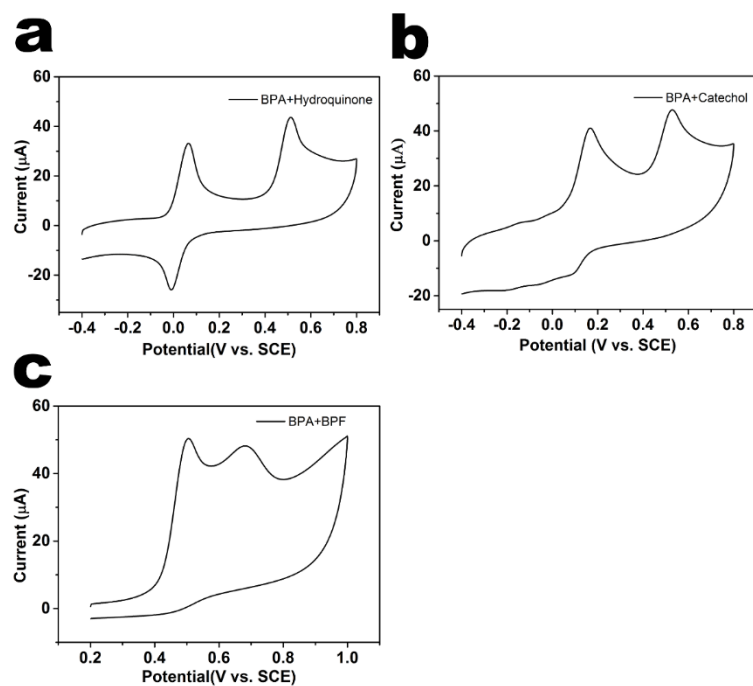


Figure S17. Cyclic voltammograms of BPA and hydroquinone (a), BPA and catechol (b), BPA and bisphenol F (BPF) (c) on GCE/CNT@mC/Pt in PBS buffer at scan rate of 100 mV s^{-1} .

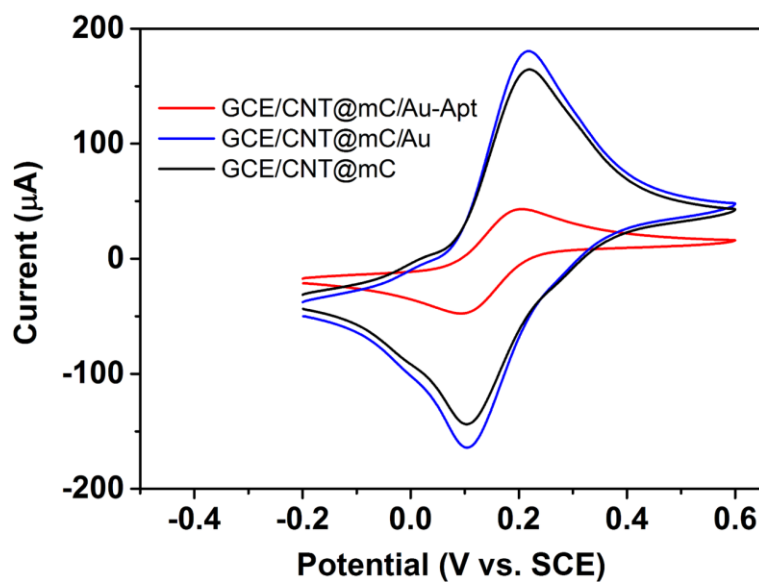


Figure S18. Cyclic voltammograms of GCE/CNT@mC, GCE/CNT@mC/Au and GCE/CNT@mC/Au-Apt in $[\text{Fe}(\text{CN})_6]^{3-/4-}$ solution.

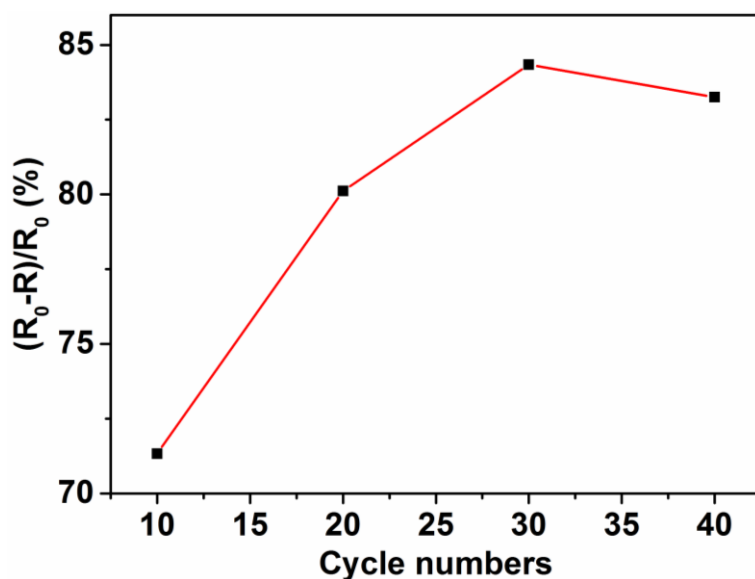


Figure S19. The changes of electron transfer resistance of GCE/CNT@mC/Au-Apt with different amounts of Au loading in $[\text{Fe}(\text{CN})_6]^{3-/4-}$ solution. Note: R_0 and R are the electron transfer resistance of GCE/CNT@mC/Au-Apt in the absence and presence of BPA, respectively.

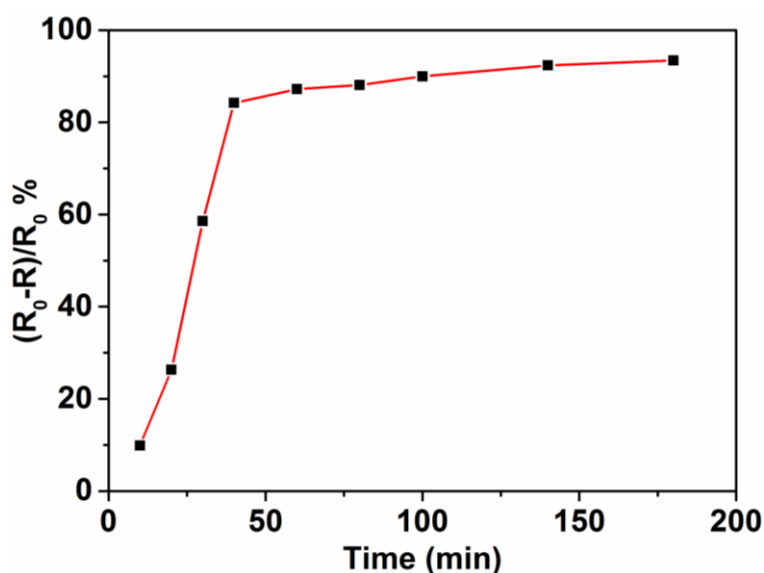


Figure S20. The changes of electron transfer resistance of GCE/CNT@mC/Au-Apt at different interaction time. Note: R_0 and R are the electron transfer resistance of GCE/CNT@mC/Au-Apt in the absence and presence of BPA, respectively.